J Vis (2015) 18:705–718
DOI 10.1007/s12650-014-0264-8

REGULAR PAPER

Hui Hu · Bing Wang · Kai Zhang · William Lohry · Song Zhang

Quantification of transient behavior of wind-driven surface droplet/rivulet flows using a digital fringe projection technique

Received: 15 September 2014 / Revised: 4 December 2014 / Accepted: 6 December 2014 / Published online: 27 December 2014

Abstract A digital fringe projection (DFP) system is developed to achieve non-intrusive thickness measurements of wind-driven water droplet/rivulet flows over a test plate to quantify the unsteady surface water transport process pertinent to various atmospheric icing phenomena. The DFP technique is based on the principle of structured light triangulation in a similar manner as a stereo vision system but replacing one of the cameras for stereo imaging with a digital projector. The digital projector projects line patterns of known characteristics onto the test specimen (i.e., a water droplet/rivulet on a test plate for the present study). The pattern of the lines is modulated from the surface of the test object. By comparing the modulated pattern and a reference image, the 3D profile of the test object with respect to the reference plane (i.e., the thickness distribution of the water droplet/rivulet flow) can be retrieved quantitatively and instantaneously. The feasibility and implementation of the DFP system is first demonstrated by measuring the thickness distribution of a small flat-top pyramid over a test plate to evaluate the measurement accuracy level of the DFP system. After carefully calibrated and validated, the DFP system is applied to achieve time-resolved thickness distribution measurements of a water droplet/rivulet to quantify the transient behavior of a water droplet/rivulet flow driven by a boundary layer air flow over a test plate. The dynamic shape changes and stumbling runback motion of the wind-driven water droplet/rivulet flow were measured in real time in terms of film thickness distribution, contact line moving velocity, wet surface area and droplet evaporation rate.

Keywords Non-intrusive measurements of film/rivulet flow · Digital fringe projection technique · Wind-driven droplet/rivulet flow · Surface water transport · Icing physics

1 Introduction

Ice accretion on cold surfaces is a topic of great concern for a number of engineering applications. Ice formation and accretion on power cable and radio masts have been found to cause significant damage or completely destroyed the electric equipment on numerous occasions (Farzaneh 2000). Aircraft icing is widely recognized as one of the most serious weather hazards to aircraft operations (Bragg et al. 1986; Gent et al. 2000). The importance of proper ice control for aircraft operation in cold climate was highlighted by many aircraft crashes in recent years like the Continental Connection Flight 3407 crashed in Buffalo, New York due to ice buildup on its wings killing all 49 people aboard and 1 person on the ground as the plane hit a residential home on February 14, 2009. Ice accretion on turbine blades was found to decrease power

H. Hu (✉) · B. Wang · K. Zhang
Department of Aerospace Engineering, Iowa State University, Ames, IA 50011, USA
E-mail: huhui@iastate.edu

W. Lohry · S. Zhang
Department of Mechanical Engineering, Iowa State University, Ames, IA 50011, USA

production of wind turbines significantly (Dalili et al. 2009), random ice accretion and irregular shedding of large chunks of ice during wind turbine operation would also lead to load imbalances, as well as excessive turbine vibration, often causing the wind turbine to shut off (Homola et al. 2006).

Advancing the technology for safe and efficient operation of numerous functional devices in atmospheric icing conditions requires a better understanding of icing physics. While a number of theoretic and numerical studies have been conducted in recent years to develop ice prediction tools for improved ice protection system designs (Hansman and Turnock 1989; Otta and Rothmayer 2009), many details of important microphysical processes that are responsible for ice formation and accretion on frozen cold surfaces are still unclear (Politovich 1989; Myers and Charpin 2004; Brakel et al. 2007; Hu and Huang 2009; Hu and Jin 2010). Advanced experimental techniques capable of providing accurate measurements to quantify the important microphysical processes pertinent to icing phenomena, such as transient behavior of surface water transport and interaction among the unfrozen surface water, the local airflow and ice, are highly desirable to elucidate the underlying physics. In this study, we report the progress made in our recent effort to develop a digital fringe project (DFP) system to achieve non-intrusive thickness measurements of wind-driven water droplet/rivulet flows over test surfaces to quantify the transient behavior of the unsteady surface water transport process pertinent to various icing phenomena found in nature. The quantitative DFP measurements are very helpful to elucidate the underlying physics for a better understanding of the important micro-physical process, which could lead to improvements of current icing accretion models for more accurate prediction of ice formation and accretion process as well as the development of effective icing mitigation and protection systems for various engineering applications.

2 Digital fringe projection (DFP) technique

Digital fringe projection technique used in the present study is a special kind of the structured light projection method, which is based on the projection of structured light patterns varying sinusoidally with respect to light intensity. While structured light projection techniques basically are stereovision methods, in DFP one of the cameras is replaced by a digital projector (Salvi et al. 2010). Similar to triangulation methods, depth information can be recovered by identifying the corresponding pairs from two different views (Geng 2011). In the present study, the pattern of lines projected onto the object was generated via digital image processing. This strategy has significant advantages over laser interference-based technology. First, measurement accuracy is not affected by speckle noise. Second, the intensity profile of the fringe pattern can be accurately controlled. Third, phase shift errors due to mechanical devices are eliminated.

Figure 1 shows the schematic of the typical setup of a DFP system. A digital projector projects line patterns of known characteristics onto the specimen under investigation (i.e., a water droplet/rivulet flow over a test plate for the present study). The projected lines are modulated by the surface of the specimen, and the modulated pattern is compared with a reference pattern to extract 3D shape of the specimen. As shown in Fig. 1, the projection unit (D), image acquisition unit (E), and the three-dimensional object (B) form a

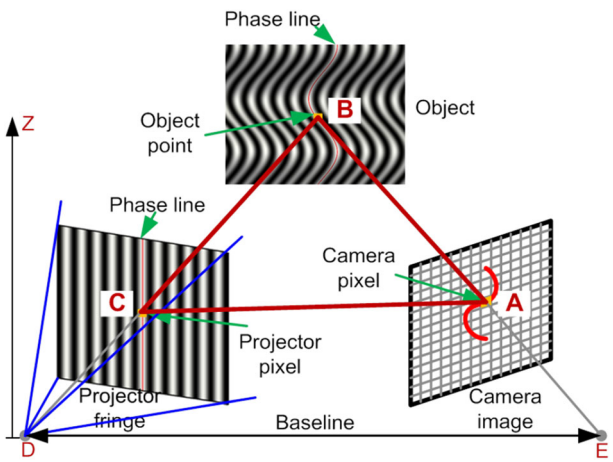

Fig. 1 Schematic of a digital fringe projection system

triangulation base. If the corresponding points between the camera (A) and the projector (C) are identified through a calibration procedure, 3D surface shape of the object can be obtained through an analysis of triangulation (ΔABC). The correspondence is established by analyzing the phase distributions of the line patterns computed via digital image processing. By comparing the phase of the modulated fringe patterns (in the present study, the water droplet/rivulet immersed in the airflow) with the phase of the reference plane, it is possible to reconstruct the 3D shape of the specimen surface.

2.1 Fourier transform-based fringe analysis procedure

As described in Takeda et al. (1982) and Takeda and Mutoh (1983), the typical fringe pattern recorded by the sensor in DFP technique is a signal with spatial carrier frequencies n/p modulated in both phase $\phi(x,\ y,\ t)$ and amplitude $A(x,\ y,\ t)$. This signal can be expressed by the Fourier expansion

$$I(x,\ y,\ t) = \sum_{n=-\infty}^{\infty} q_n(x,\ y,\ t)\exp(j2\pi ny/p) \tag{1}$$

with:

$$q_n(x,\ y,\ t) \ = \ A_n(x,\ y,\ t)\exp[jn\phi(x,\ y,\ t)] \tag{2}$$

where, j is the imaginary unit, and $A_n(x,\ y,\ t)$ is the amplitude modulation due to the light source and inhomogeneous surface reflectivity of the test object. The phase $\phi(x,y,t)$ contains the 3D shape information on the test object shape, p is the fringe pitch on the reference plane. The zero frequency intensity value corresponds to the background intensity variation over the field of view. Since the phase carries information on the 3D shape to be measured, the strategy would be to separate the phase $\phi(x,y,t)$ out from the intensity signal.

Using discrete Fourier Transfer in the spatial domain, the spectrum of intensity distribution $I(x,y,t)$ recorded by sensor at a certain instant can be obtained. Since $A_n(x,y,t)$ and $\phi(x,y,t)$ usually vary much less compared with the spatial frequency of the fringe given by $1/p$, all the spectra can be well separated from each other. A filtering operation can be performed to extract the spectrum of the fundamental frequency component, and compute its inverse Fourier transform to obtain a complex signal as written below

$$\widehat{I}(x,y,t) \ = \ A_1(x,y,t)\exp\{j[2\pi y/p + \phi(x,y,t)]\} \tag{3}$$

The same signal processing can also be done for the reference fringe image to obtain

$$\widehat{I}_0(x,y) = \mathcal{A}(x,y)\exp\{j[2\pi y/p + \phi_0(x,y)]\} \tag{4}$$

Then the phase difference between the modulated pattern and the reference image can be extracted from a new signal expressed as

$$\widehat{I}(x,y,t)\cdot\widehat{I}_0^*(x,y) \ = \ A_1(x,y,t)\mathcal{A}(x,y)\exp\{j[\Delta\phi(x,y,t)]\} \tag{5}$$

where $*$ indicates complex conjugate of the signal, and $\Delta\phi(x,y,t) = \phi(x,y,t) - \phi_0(x,y)$ is the phase difference between the deformed fringes over the object and the reference fringes. The phase difference can be computed from the ratio between the imaginary and real part of the new signal as written below

$$\Delta\phi(x,y,t) = \arctan\left\{Im\left[\widehat{I}(x,y,t)\cdot\widehat{I}_0^*(x,y)\right]/Re\left[\widehat{I}(x,y,t)\cdot\widehat{I}_0^*(x,y)\right]\right\} \tag{6}$$

Since the phase map computed from Eq. (6) is wrapped in the $[-\pi/2, \pi/2]$ range, phase unwrapping must be performed to obtain a continuous phase map. The phase unwrapping step consists of finding the 2π jumps from neighboring pixels, and removing them by adding or subtracting an integer number of 2π to the corresponding point (Ghiglia and Pritt 1998). In other words, the phase unwrapping algorithm must determine an integer number $k(x,y)$ such that

$$\Phi\Delta(x,y,t) = \Delta\phi(x,y,t) \ + \ 2\pi\cdot k(x,y) \tag{7}$$

In Eq. (7), $\Phi\Delta(x,y,t)$ is the unwrapped phase map. Once the unwrapped phase map is known, the 3D coordinates of the object surface can be determined, assuming that the system is properly calibrated (Zhang and Huang 2006).

It should be noted that, while the Fourier transform method is the "natural" single frame-based fringe analysis technique used in the present study, more advanced methods such as phase shifting techniques have

been developed for interferometry measurements (Bruning et al. 1974; De Groot 1995; Surrel 1996 and Phillion 1997). In addition, developments have also been done in dynamic phase shifting, either it be with adapted algorithm able to take into account different types of errors (Colonna de Lega and Jacquot 1996), or using color to parallelize the phase-shifted images capture (Wust and Capson 1991).

2.2 Phase-to-height conversion algorithm

The 3D surface shape of the object can be extracted from the unwrapped phase map if the DFP system is properly calibrated. To convert the phase map to height distribution, the relationship between the height and the phase must be established. Figure 2 shows the principle schematic of the measurement system implemented in the present study. A reference plane with height 0 in the Z-direction is used as the reference for subsequent measurement (i.e., the surface of test plate for the present study). The arbitrary point M in the captured image corresponds to point N in the projected image, and point D on the object surface (i.e., on the free surface of the droplet/rivulet flow for the present study). From the projector's point of view, phase Φ_D on the object surface has the same phase value as Φ_A on the reference plane, that is, $\Phi_A = \Phi_D$. While from the point of view of the CCD camera, point D on the object surface images is at the same pixel as point C on the reference plane. The phase difference between point C on the reference plane and point D on the object can be expressed as:$\Phi_{CD} = \Phi_{CA} = \Phi_C - \Phi_A$. Assume the distance between point M and point N is d, and the reference plane is parallel to the device with a distance s between them. By analyzing the similar relationship between ΔMND and ΔCAD, we can get:

$$\frac{d}{\overline{CA}} = \frac{s - \overline{BD}}{\overline{BD}} = \frac{s}{\overline{BD}} - 1 \tag{8}$$

In DFP measurements, the distance s is usually much larger than $\overline{BD}$, therefore, the equation can be simplified as:

$$Z(x, y) = \overline{BD} \approx \frac{s}{d}\overline{CA} = \frac{ps}{2\pi d}\phi_{CA} \tag{9}$$

where p is the pitch of the projected line pattern in the reference plane. From above equation, it can be seen that a linear relationship between the phase difference, Φ_{CA}, and the height information, $Z(x, y)$, can be obtained. Therefore, the 3D shape of the specimen surface can be precisely determined by measuring the phase difference between the modulated and reference images.

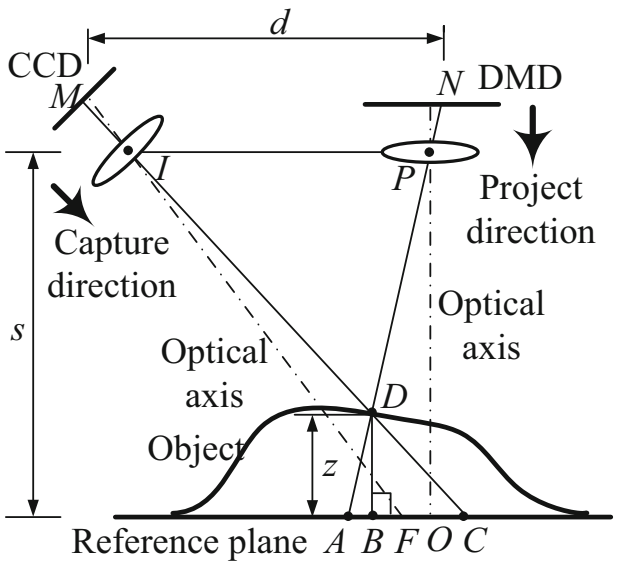

Fig. 2 Schematic diagram of the phase-to-height conversion

2.3 Binary defocusing technique

While a conventional DFP system may work well for static or quasi-static 3D shape measurements, there are several issues in time-resolved measurements like those carried out in the present study to characterize the transient behavior of wind-driven water droplets/rivulet flows over smooth/rough surface for icing physics studies. For example, precise synchronization, nonlinearity, and limitation on maximum speed (Lei and Zhang 2010). The core of a digital-light processing (DLP) projector is a digital micro-mirror device (DMD). Each micro-mirror can rotate between $+\theta L$ (ON) and $-\theta L$ (OFF). The grayscale value of each pixel is realized by controlling the ON time ratio: for an 8-bit system, 0 % ON time represents 0, 50 % ON time means 128, and 100 % ON time is 255. Therefore, a DLP projector produces a grayscale value by time modulation. As a result, for a conventional DFP system where the sinusoidal fringe patterns are fed to the projector, the camera must be precisely synchronized with projector to correctly capture the projected patterns. A conventional DMD is usually fed with an intensity value of 0 or 255 and remains its status (without flipping ON/OFF) during the period of channel projection. Using binary patterns (i.e. 0 and 255 s) instead of sinusoidal structured patterns, it is possible to set an arbitrary exposure time for the camera. Since sinusoidal line patterns allow 3D shape contouring to be performed with DFP, a flexible method was recently developed to generate sinusoidal patterns by defocusing binary patterns (Lei and Zhang 2009). When a projector is fed with binary structured patterns and their focal length is changed, the projected structured patterns that are initially focused are gradually transformed into sinusoidal patterns that are out-of-focus. In this way, it is possible to eliminate problems deriving from projector nonlinearity. Although numerous nonlinearity calibration approaches have been developed, it remains difficult for a conventional projector to generate ideal sinusoidal patterns. Since the binary defocusing technique only requires two intensity values, nonlinearity problems disappear. In addition, because of the use of 1-bit binary patterns, it is possible to perform super-high-speed 3D shape imaging. In the present study, the binary defocusing technique was used to generate sinusoidal line patterns thus increasing significantly the temporal resolution of DFP measurements.

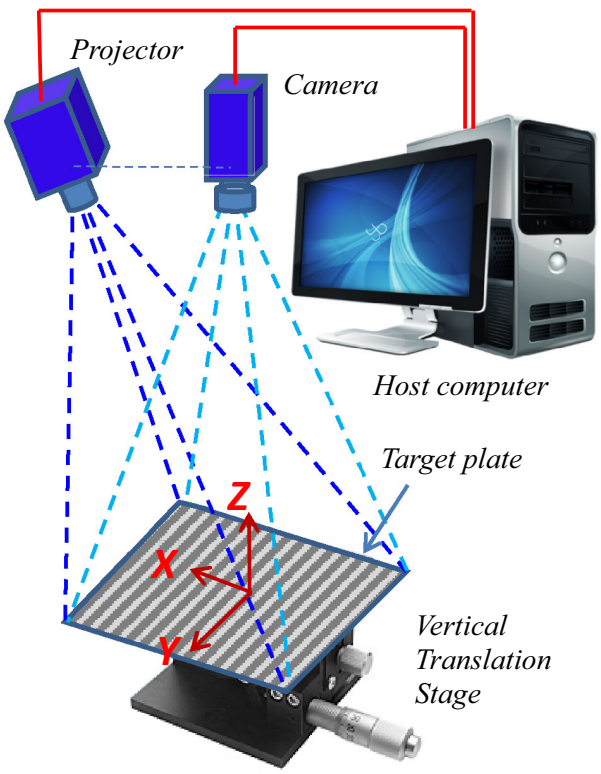

Fig. 3 Experimental setup for DFP calibration

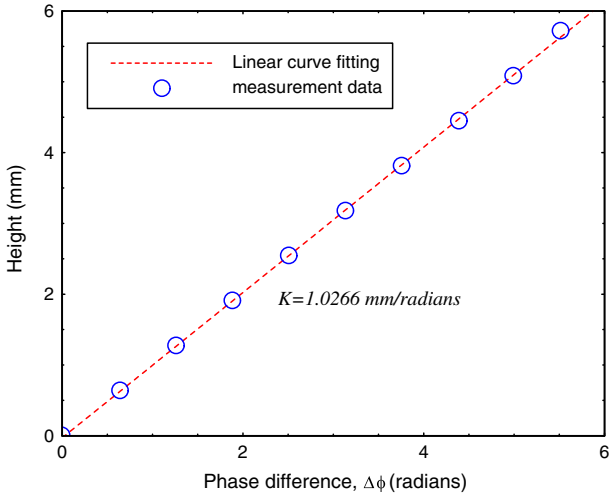

Fig. 4 Calibration curve to determine the phase-to-height conversion coefficient

2.4 Experimental setup for calibration

The relationship between phase and depth was determined through calibration. Figure 3 shows the schematic setup of the calibration procedure employed in the present study. A binary blank/white fringe image was generated artificially using MATLAB software on a host computer. A portable digital projector (Dell M109S DLP SVGA Projector) was used to project the binary fringe image onto a test plate (100 mm × 100 mm in size), which is about 1,200 mm away from the projector. The test plate was mounted on the top of a vertical translation stage, and the height of the vertical translation stage (i.e., the position of the test plate along Z-direction) was adjusted using a micrometer drive with a resolution of 10 μm. The focal plane of the digital projector was adjusted to be off the test plate to use the binary defocusing technique for generating sinusoidal fringe patterns on the test plate. A progressive scan CCD camera (DMK21BU04, Imaging Source Corp.) was used to record the images of the projected fringe patterns on the test plate. The recorded images were stored on the host computer for DFP image processing.

In the calibration procedure, a translation stage moved vertically the test plate through ten different positions along the Z-direction; those positions were uniformly spaced by 0.5 mm. The sinusoidal pattern projected onto the test plate was recorded for each position and then processed in the Fourier space. For each position, the phase shift of the pattern was calculated with respect to the reference plane (i.e., the phase difference from the initial position corresponding to $Z = 0$). Figure 4 shows the variation of the phase shift as the test plate is moved away from its original position. The relationship between the height (i.e., the distance from the reference plane) and the phase difference is well fitted by a linear function, in agreement with Eq. (9). The constant of proportionality K derived from the calibration procedure was used for the phase-to-height conversion in the DFP measurements carried out in this study.

3 Measurement of the 3D shape of a mini flat-top pyramid

To demonstrate the feasibility and implementation of the proposed DFP technique, the 3D shape (i.e. thickness distribution) of a mini flat-top pyramid was measured using the DFP technique described above. The nominal dimensions of the specimen are: height of 4.7 mm, square base side of 15 mm, sides inclined by 45° with respect to the vertical axis. The experimental setup utilized in the contouring of the mini-pyramid is the same as that used for the calibration procedure. The specimen was placed in the center of the test plate.

Figure 5 shows the typical measurement results along with the acquired DFP raw images. Figure 5(a) shows the reference pattern formed by a set of straight lines projected onto the test plate without placing the specimen. The projected lines are then modulated by the mini-pyramid placed on the reference plane, as shown in Fig. 5b. Phase maps can be computed for the reference image and the modulated pattern: in particular, Fig. 5c shows the wrapped phase map obtained for the modulated pattern. Figure 5d shows the

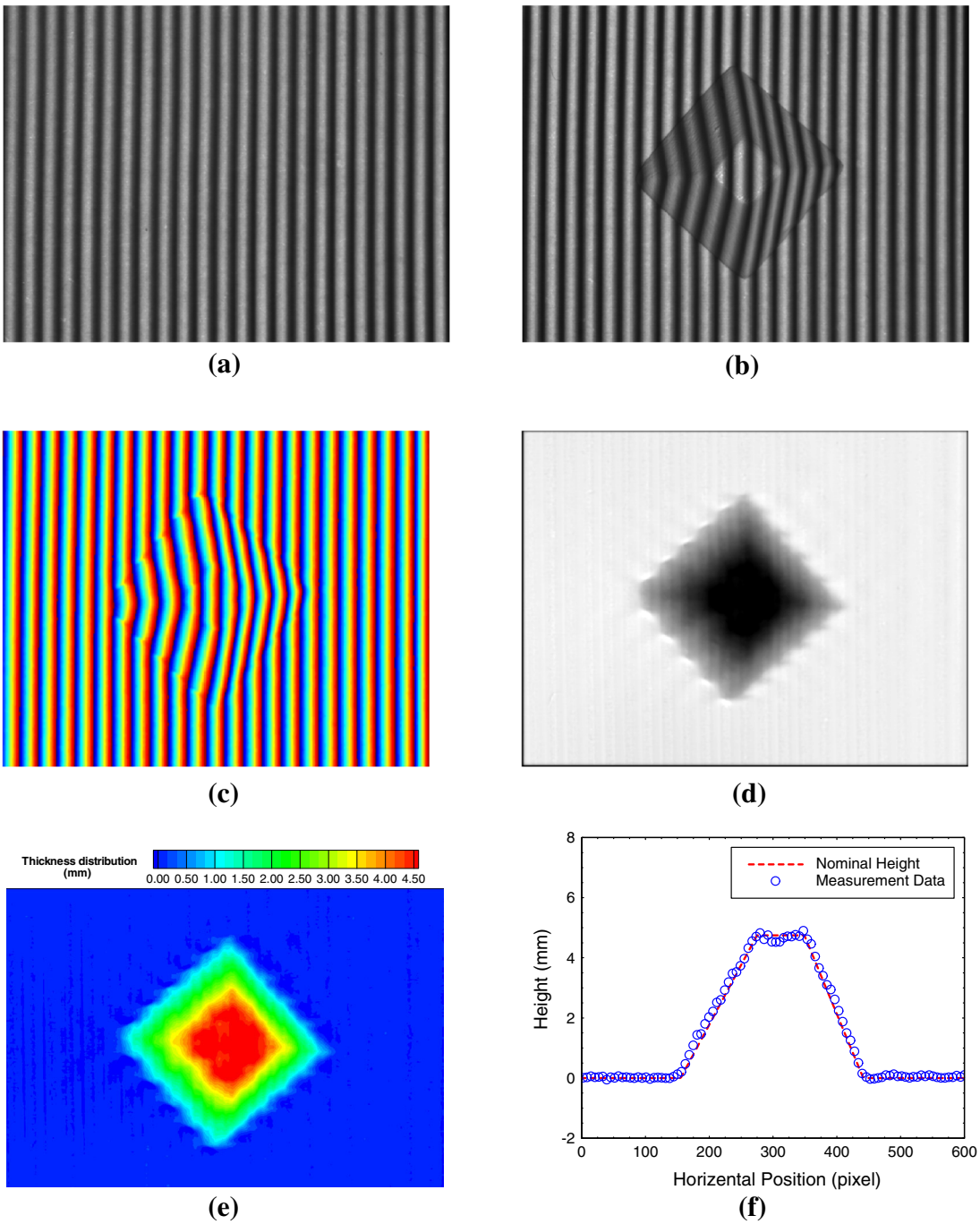

Fig. 5 DFP measurement of a mini flat-top pyramid. **a** Reference images without pyramid. **b** Projected line pattern modulated by the pyramid. **c** Wrapped phase map of the modulated image.**d** The phase difference map. **e** Derived height distribution of the pyramid. **f** The measured height vs. nominal height

results of the subtraction of the unwrapped phases of the object and reference plane. The height distribution of the mini-pyramid, as shown in Fig. 5e, can be determined using the phase-to-height conversion relationship determined through calibration.

Since the nominal height distribution of the pyramid was known, the measurement accuracy of the DFP system was evaluated by comparing the measured height distribution with the nominal shape of the specimen. Figure 5f compares the measured height with the nominal profile of the pyramid along a control path corresponding to a horizontal line passing through the center of the specimen. While the measured profile

matches reasonably well the nominal profile, the measurement error is larger in the regions where there are sharp changes in object geometry (for example, near the boundaries of the mini-pyramid). It can be seen clearly that measurement uncertainty is relatively high on the flat top of the pyramid due to the poor spatial resolution of projected lines in the flat-top region. Since the optimal value of the pitch of the projected line pattern must ensure high spatial resolution and good quality of the recorded images (these issues may indeed conflict), a systematic study should always be carried out to evaluate the effects of the important parameter settings, such as the pitch of the projected lines, angle of illumination, baseline distance, distance between projector, camera and object, etc., on the measurement uncertainty levels of a DFP system. For the DFP measurement results given in Fig. 5, the root mean square value of the measurement errors was found to be about 0.16 mm, which is about 3 % of the nominal height of the pyramid (i.e., 4.7 mm).

4 Quantification of the transient behavior of a wind-driven water droplet/rivulet flow

The DFP system was then used to quantify the transient behavior of the water droplet/rivulet flow driven by a boundary layer wind over a test plat to elucidate the underlying physics of the surface water transportation process pertinent to various atmospheric icing phenomena. Figure 6 shows the schematic of the experimental setup used in the present study. The DFP measurements were performed in a low-speed wind tunnel located in the Department of Aerospace Engineering, Iowa State University. The digital projector, the CCD camera and a flat test plate were arranged in the same manner as those used in the calibration experiments. The test plate was flush mounted on the bottom surface of the test section of the wind tunnel. The temperature of the test plate can be adjusted using a water bath Circulator (Neslab RTE-211). Since the main objective of the present study is to demonstrate the feasibility and implementation of the DFP technique described for time-resolved film thickness distribution measurements to quantify unsteady wind-driven droplet/rivulet flows, the test plate was kept at room temperature (i.e., T = 23.0 $^{\circ}$C, thus, no ice formation) during the experiments.

In the present study, water was employed as the working liquid. Following the work of Cabelli et al. (2009), a small amount of white liquid dye was added into the water to enhance the contrast of the projected fringes onto the free surfaces of the water droplets/rivulets. Driven by the incoming boundary layer airflow, the water droplet on the test plate would deform and run back to form film/rivulet flows. This simulates the surface water transportation process during glaze ice formation and accretion process over a frozen cold aircraft wing or wind turbine blade, i.e., after impinging onto the surface of an aircraft wing or turbine blade, tiny super-cold water droplets aggregate to form larger droplets/rivulets and run back upon the pushing of the boundary layer airflow during glaze ice formation and accretion process.

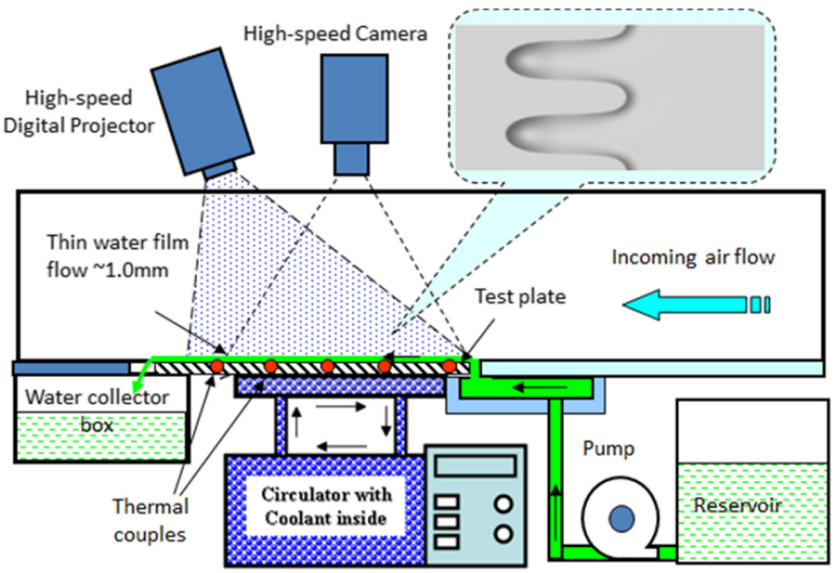

Fig. 6 Experimental setup to quantify unsteady wind-driven droplet/rivulet flows

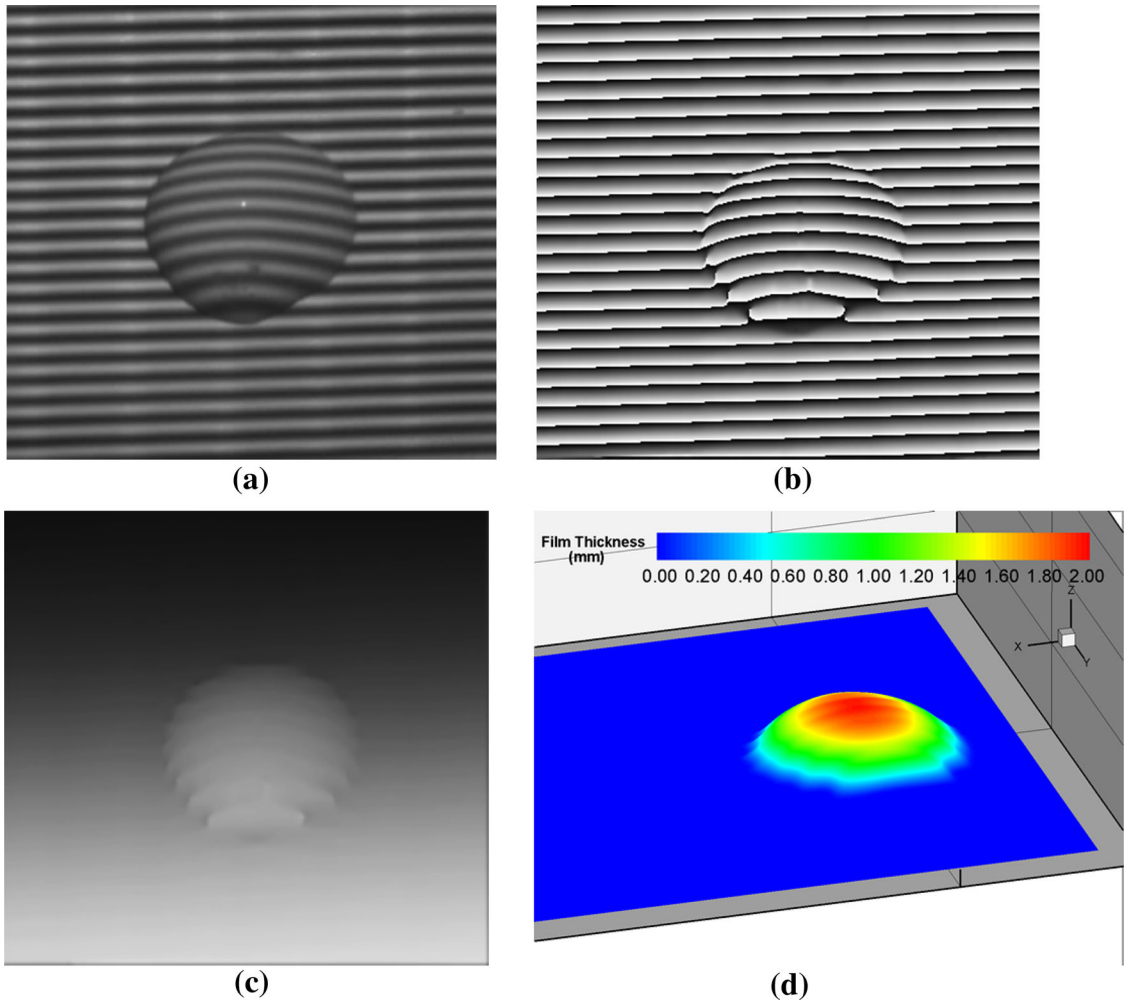

Fig. 7 Results of DFP measurements carried out on a water droplet not immersed in the airstream. **a** DFP raw image. **b** Wrapped phase map. **c** Unwrapped phase map. **d** Derived height distribution

Figure 7 shows the results of the DFP measurements carried out for a water droplet of about 10.0 mm in diameter lying on the test plate. Measurements were conducted without turning on the wind tunnel. As expected, the water droplet was found to be round sphere cap shape on the test plate. This can be seen clearly from the raw DFP image, the wrapped and unwrapped phase maps as well as the measured thickness distribution of the water droplet.

Figure 8 shows the time sequence of the DFP measurements to reveal the dynamic shape changes of the water droplet immersed in an airflow with free stream velocity of $V_\infty = 10.0$ m/s. The raw DFP images recorded by the sensor at 60 Hz frame rate are shown in the left part of the figure. The corresponding thickness distributions are shown in the right part of the figure. It can be seen clearly that the projected pattern initially formed by straight lines was dynamically modulated to follow the dynamic shape changes of the water droplet/rivulet flow driven by the boundary layer airflow. As the water droplet runs back upon the pushing of the boundary layer airflow, a tail of the droplet would leave behind the moving droplet to form a thin film over the test plate. The shape of the water droplet changed from round sphere cap to sand dune shape, and finally became a thin film/rivulet flow spreading out over the test plate.

The velocity of the contact line between the droplet/rivulet flow and the test plate can be determined from the time sequence of DFP measurements as those shown in Fig. 8. Figure 9 shows the time variation of the moving velocity of the contact lines corresponding to the front lobe and rear end of the droplet/rivulet. Even though the boundary layer airflow was kept constant throughout experiments, the runback motion of the wind-driven droplet/rivulet flow over the test plate was found to be quite unsteady. In fact, the droplet/rivulet flow was found to stumble over the test plate, instead of moving smoothly and continuously.

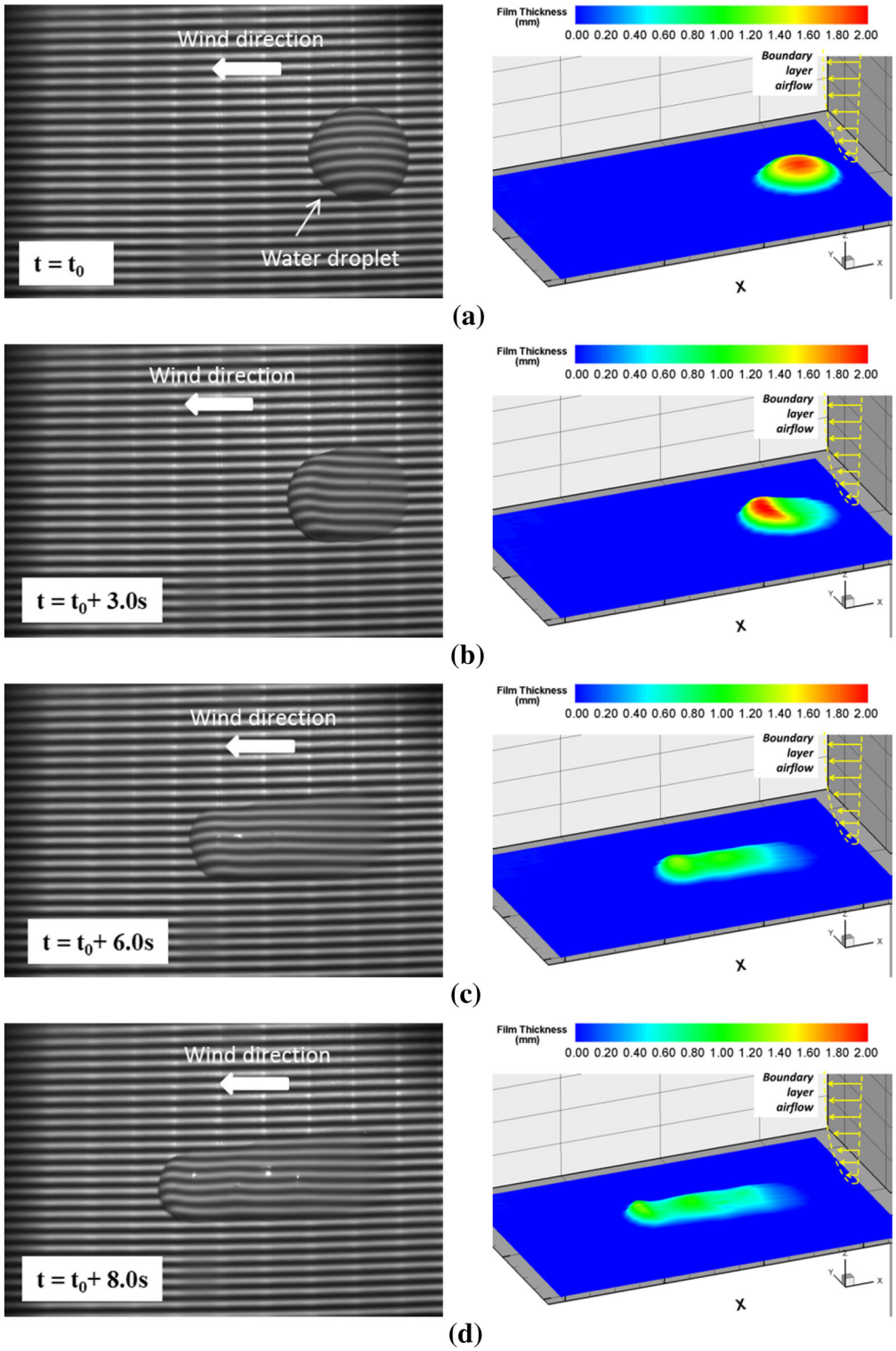

Fig. 8 Time sequence of the DFP measurement results to quantify the evolution of a wind-driven water droplet/rivulet flow. **a** $t = t_0 + 0.0$ s , **b** $t = t_0 + 3.0$ s, **c** $t = t_0 + 6.0$ s, **d** $t = t_0 + 8.0$ s

Figure 10 shows the time evolution of the central line profile of the wind-driven droplet/rivulet flow over the test plate, which can reveal the dynamic shape changes and stumbling runback motion of the water droplet/rivulet flow more clearly. It can be seen clearly that, both the front and rear contact lines of the

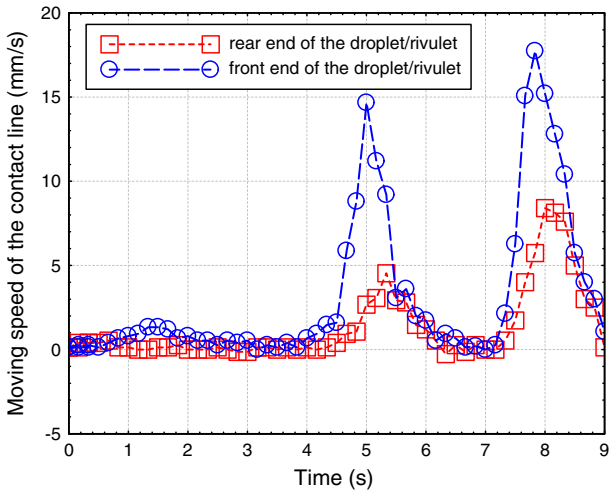

Fig. 9 Time evolution of contact line velocities of the *front lobe* and *rear end* of the wind-driven droplet/rivulet flow

droplet/rivulet were found to move very slowly or almost do not move at all at the beginning (i.e., $t < 4.5$ s), while the free surface of the droplet/rivulet was found to deform dramatically to change its shape from round sphere cap to sand dune shape (i.e., Fig. 10a–e). The front lobe of the deformed droplet/rivulet was found to skip suddenly downstream at the time of $t \approx 4.5$ s (Fig. 10f), and the contact line moving velocity of the droplet/rivulet rapidly increases corresponding to the "skip" motion, which is consistent with the measurement data given in Fig. 9. The droplet/rivulet then rest in its new position for a while (i.e., the contact line moving velocity of the droplet/rivulet again turns quite small at 5.5 s $< t <$ 7.0 s) before it "skipped" again to run back further downstream (Fig. 10g, h). Due to the pushing of the boundary layer airflow, wave structures were found to form on the free surface of the droplet/rivulet flow, which propagate from the front lobe back to the rear end of the droplet/rivulet flow, as shown clearly in Fig. 10i, j). Then, the water sloshes back to the front lobe, thus pushing the droplet/rivulet to lurch forward. As shown clearly in Fig. 9, the moving velocity of the contact line at the front lobe of the droplet/rivulet was found to be always higher than that at the rear end of the droplet/rivulet. It indicates that the wind-driven droplet/rivulet spreads out over the test plate, as expected.

Based on the time-resolved DFP measurements as those given above, the time evolution of the dynamic contact angles of the wind-driven droplet/rivulet flow (results are not shown here) and the wet surface area (i.e., the spreading area of the droplet/rivulet over the test plate) can also be determined from the quantitative data gathered with DFP measurements. Figure 11 shows the measured wet surface area of the droplet/rivulet flow as a function of time: this parameter can be used to quantify the spreading extent of the wind-driven droplet/rivulet flow over the test plate. As expected, the wet surface area of the droplet/rivulet flow over the test plate increases monotonically with time. Interestingly, instead of increasing smoothly and continuously, the wet surface area shows a stepped increasing trend. This behavior is closely related to the stumbling motion of the wind-driven droplet/rivulet flow: each "skip" of droplet/rivulet flow in the stumbling runback process corresponds to a jump to increase the wet surface area of the droplet/rivulet flow.

From the measured thickness distribution and wet surface area of the droplet/rivulet flow over the test plate, the total volume (hence, mass) of the water droplet/rivulet flow also can be determined quantitatively. This volume is also shown in Fig. 11. As expected, the total volume of the water droplet/rivulet was found to decrease monotonically due to evaporation. Since a larger wet surface area of the droplet/rivulet flow over the test plate implies a stronger evaporation of the water droplet/rivulet flow, as a result, the volume of the droplet/rivulet was found to decrease more rapidly as the wet surface area of the droplet/rivulet over the test plate increases, which was also confirmed from the time-resolved DFP measurement results given in Fig. 11.

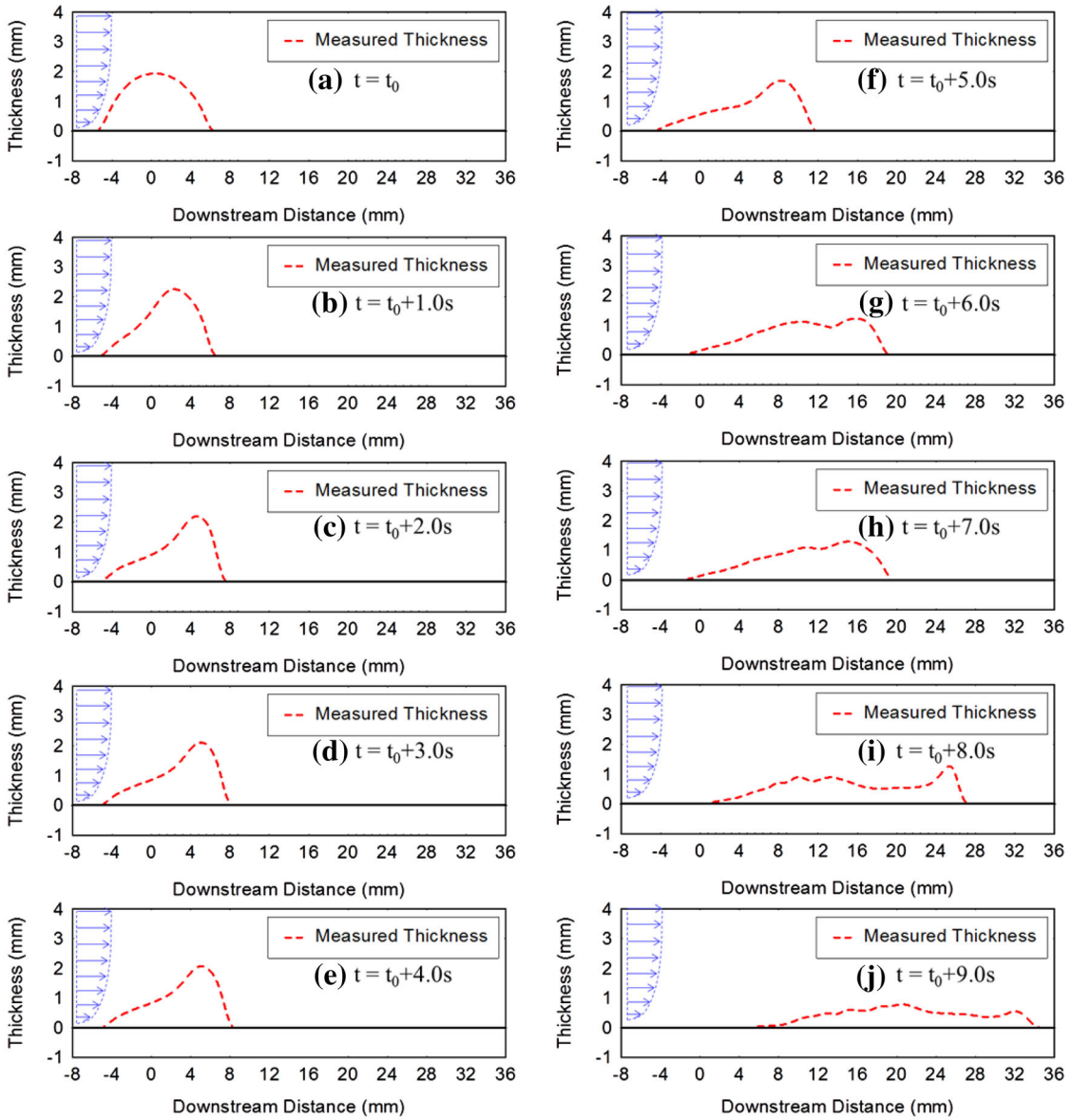

Fig. 10 Time evolution of the wind-driven droplet/rivulet flow over the test plate

5 Conclusions

In the present study, a digital fringe projection (DFP) system was developed to measure in real time the thickness distribution of wind-driven water droplet/rivulet flows spreading over planar surfaces to elucidate underlying physics to improve our understanding about the unsteady surface water transportation process over a solid surface pertinent to various atmospheric icing phenomena. The DFP technique utilized in this study is a special structured light projection method based on the triangulation principle: one of the cameras for stereo imaging is replaced by a digital projector. The projector projects line patterns of known characteristics onto the specimen that in the present case was the water droplet/rivulet flowing over the test plate. The pattern of lines is modulated from the surface of the test object. By comparing the phase differences between the modulated fringe patterns over the test object and a reference fringe pattern on the reference plane, the 3D shape of the object under investigation with respect to the reference plane (i.e., the thickness distribution of the water droplet/rivulet flow over the test plate) was retrieved quantitatively and instantaneously.

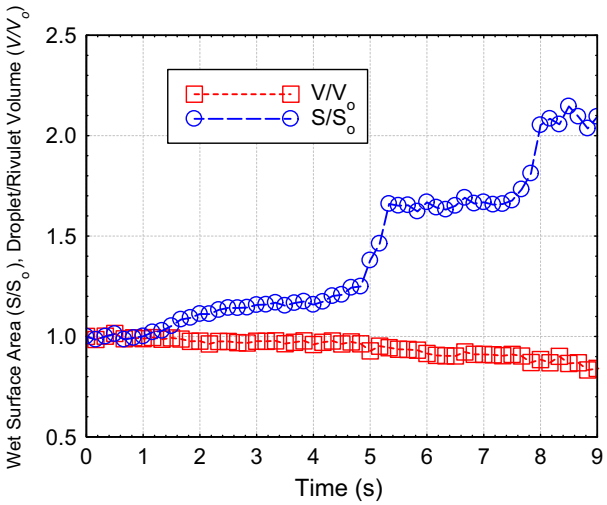

Fig. 11 Time evolution of the measured wet surface area and total volume of the wind-driven droplet/rivulet flow over the test plate

The feasibility and implementation of the DFP technique were first demonstrated by measuring the thickness distribution of a small flat-top pyramid. The DFP measurement results were compared with the nominal height distribution of the pyramid quantitatively to evaluate the measurement uncertainty of the DFP system. With the parameter settings used in the present study, the measurement uncertainty of the DFP system was found to be less than 160 μm, which is about 3 % of the nominal height of the flat-top pyramid.

After carefully calibrated and validated, the DFP system was utilized to measure the dynamic shape changes of a water droplet/rivulet flow driven by boundary layer airflow over a test plate. Dynamic shape changes and stumbling runback motion of the water droplet/rivulet were measured in real time in terms of film thickness distribution, contact line moving velocity, wet surface area and droplet evaporation rate. The large amount of information gathered with respect to time is very useful to elucidate underlying physics to improve our understanding about the surface water transport process pertinent to ice formation and accretion over solid surfaces in atmospheric icing conditions. The present study can be a good start point towards the development of effective anti-/de-icing strategies tailored for safer and more efficient operation of various functional devices in cold weather.

Acknowledgments The research work is partially supported by National Aeronautical and Space Administration (NASA)—Grant number NNX12AC21A with Mr. Mark Potapczuk as the technical officer and Iowa Space Grant Consortium (ISGC) Base Program for Aircraft Icing Studies with Dr. Charisse Buising as the Director. The support of National Science Foundation (NSF) under award numbers of CBET-1064196 and CBET-1435590 is also gratefully acknowledged.

References

Bragg M, Gregorek G, Lee J (1986) Airfoil aerodynamics in icing conditions. J Aircr 23(1):76–81

Brakel TW, Charpin JPF, Myers TG (2007) One-dimensional ice growth due to incoming supercooled droplets impacting on a thin conducting substrate. Int J Heat Mass Transf 50:1694–1705

Bruning JH, Herriott DR, Gallagher JE, Rosenfeld DP, White AD, Brangaccio DJ (1974) Digital wavefront measuring interferometer for testing optical surfaces and lenses. Appl Opt 13(11):2693–2703

Cobelli PJ, Maurel A, Pagneux V, Petitjeans P (2009) Global measurement of water waves by Fourier transform profilometry. Exp Fluids 46:1037–1047

Colonna De Lega X, Jacquot P (1996) Deformation measurement with object-induced dynamic phase shifting. Appl Opt 35(25):5115–5121

Dalili N, Edrisy A, Carriveau R (2009) A review of surface engineering issues critical to wind turbine performance. Renew Sustain Energy Rev 13(2):428–438

De Groot P (1995) Derivation of algorithms for phase-shifting interferometry using the concept of a data-sampling window. Appl Opt 34(22):4723–4730

Farzaneh M (2000) Ice accretions on high-voltage conductors and insulators and related phenomena, philosophical transactions of the royal society of London. Ser A Math Phys Sci 358(1776):2971–3005

Geng ZJ (2011) Structured-light 3D surface imaging: a tutorial. Adv Opt Photonics 3(2):128–160

Gent RW, Dart NP, Cansdale JT (2000) Aircraft icing. Phil. Trans. R. Soc. Lond. A 358:2873–2911

Ghiglia DC, Pritt MD (1998) Two-dimensional phase unwrapping: Theory, algorithms, and software. John Wiley and Sons Inc, New York
Hansman RJ, Turnock SR (1989) Investigation of surface water behavior duiring glaze ice accretion. J Aircr 26(2):140–147
Homola MC, Nicklasson PJ, Sandsbo PA (2006) Ice sensors for wind turbines". Cold Reg Sci Technol 46(2):125–131
Hu H, Huang D (2009) Simultaneous measurements of droplet size and transient temperature within surface water droplets. AIAA J 47(4):813–820
Hu H, Jin Z (2010) An Icing Physics Study by using Lifetime-based Molecular Tagging Thermometry Technique International Journal of Multiphase Flow 36(8):672–681
Lei S, Zhang S (2009) Flexible 3-D shape measurement using projector defocusing. Opt Lett 34(20):3080–3082
Lei S, Zhang S (2010) Digital sinusoidal fringe generation: defocusing binary patterns vs focusing sinusoidal patterns. Opt Lasers Eng 48(5):561–569
Myers TG, Charpin JPF (2004) A mathematical model for atmospheric ice accretion and water flow on a cold surface. Int J Heat Mass Transf 47:5483–5500
Otta SP, Rothmayer AP (2009) Instability of stagnation line icing. Comput Fluids 38(2):273–283
Phillion DW (1997) General methods for generating phase-shifting interferometry algorithms. Appl Opt 36(31):8098–8115
Politovich MK (1989) Aircraft icing caused by large supercooled droplets. J Appl Meteorol 28:856–868
Salvi J, Fernandez S, Pribanic T, Llado L (2010) A state of the art in structured light patterns for surface profilometry. Pattern Recogn 43:2666–2680
Surrel Y (1996) Design of algorithms for phase measurements by the use of phase stepping. Appl Opt 35(1):51–60
Takeda M, Mutoh K (1983) Fourier transform profilometry for the automatic measurement of 3-D object shapes. Appl Opt 22(24):3977–3982
Takeda M, Ina H, Kobayashi S (1982) Fourier-transform method of fringe-pattern analysis for computer-based topography and interferometry. J. Opt. Soc. Am. 72(1):156–160
Wust C, Capson DW (1991) Surface profile measurement using color fringe projection. Mach Vis Appl 4(3):193–203
Zhang S, Huang PS (2006) High-resolution real-time three-dimensional shape measurement. Opt Eng 45(12):123601